Journal of Materials Chemistry A

ROYAL SOCIETY OF CHEMISTRY

PAPER

View Article Online
View Journal | View Issue

Cite this: J. Mater. Chem. A, 2022, 10, 12079

Scalable and thermally-integrated solar water-splitting modules using Ag-doped Cu(In,Ga)Se_2 and NiFe layered double hydroxide nanocatalysts†

İlknur Bayrak Pehlivan,[a] Nicole A. Saguì,[a] Johan Oscarsson,[b] Zhen Qiu,[ac] Walter Zwaygardt,[d] Minoh Lee,[e] Martin Mueller,[d] Stefan Haas,[e] Lars Stolt,[b] Marika Edoff[f] and Tomas Edvinsson *[a]

Photovoltaic (PV) electrolysis is an important and powerful technology for environmentally-friendly fuel production based on solar energy. By directly coupling solar cell materials to electrochemical systems to perform water electrolysis, solar energy can be converted into hydrogen fuel utilizing locally-generated heat and avoid losses from DC–DC convertors and power grid transmission. Although there have been significant contributions to the photoelectrochemical and PV-electrolysis field using isolated laboratory cells, the capacity to upscale and retain high levels of efficiency in larger modules remains a critical issue for widespread use and application. In this study, we develop thermally-integrated, solar-driven water-splitting device modules using AgCu(In,Ga)Se_2 (ACIGS) and an alkaline electrolyzer system with NiFe-layered double hydroxide (LDH) nanocatalysts with devices of 82–100 cm^2 area. The Ga-content in the ACIGS solar cells is tuned to achieve an optimal voltage for the catalyst system, and the average efficiencies and durability of the PV-electrolyzer were tested in up to seven-day indoor and 21 day outdoor operations. We achieved a solar-to-hydrogen (STH) module efficiency of 13.4% from gas volume measurements for the system with a six-cell CIGS-electrolyzer module with an active area of 82.3 cm^2 and a 17.27% PV module efficiency under 100 mW cm^{-2} illumination, and thus 77% electricity-to-hydrogen efficiency at one full sun. Outdoor tests under mid-Europeen winter conditions exhibited an STH efficiency between 10 and 11% after the initial activation at the installation site in Jülich, Germany, in December 2020, despite challenging outdoor-test weather conditions, including sub-zero temperatures.

Received 15th February 2022
Accepted 11th May 2022

DOI: 10.1039/d2ta01252a

rsc.li/materials-a

Introduction

The development of sustainable and renewable energy sources is an important topic wherein materials selection, and process technologies must consider raw material abundance and costs to meet rising global energy demand in conjunction with their large-scale employment to reduce greenhouse gas emissions. Photovoltaics (PVs) and wind power have recently become cost-effective technologies relative to coal-, oil-, and gas-generated electricity in many parts of the world. Sunlight and wind are intermittent, however, and storage of their energy for later use is critical to effective utilization of these energy sources. Hydrogen is here a promising, carbon-free energy carrier due to its high energy density per mass and long-term storage capabilities. Comparative techno-economic analyses between photo-electrochemical water-splitting and PV-driven electrolyzers show that the latter offers greater benefits, providing higher efficiency, being cost-effective, and being part of an already commercially-available system.[1] In PV-electrolysis, water is split into molecular hydrogen and oxygen by charge generation from the solar photons in a semiconductor material and the subsequent use of these and holes in electrolysis. Both approaches benefit a system with a catalyst in direct contact with the solar cell materials.

Alkaline electrolysis can be described in terms of two half-reactions, namely: $2H_2O + 2e^- \rightarrow H_2 + 2OH^-$ (hydrogen evolution reaction, HER) and $2OH^- \rightarrow \frac{1}{2}O_2 + H_2O + 2e^-$ (oxygen evolution reaction, OER), which constitute the most widespread industrial water electrolysis technique[2,3] and carry advantages

[a]Department of Materials Science and Engineering, Solid State Physics, Uppsala University, Box 35, 75103 Uppsala, Sweden. E-mail: tomas.edvinsson@angstrom.uu.se
[b]Solibro Research AB, Vallvägen 5, 75651 Uppsala, Sweden
[c]Department of Chemical Engineering, KTH Royal Institute of Technology, SE-100 44, Stockholm, Sweden
[d]Forschungszentrum Juelich GmbH, Institute of Energy and Climate Research, IEK-14: Electrochemical Process Engineering, 52425 Juelich, Germany
[e]Forschungszentrum Juelich GmbH, Institute of Energy and Climate Research, IEK-5: Photovoltaik, Juelich 52425, Germany
[f]Department of Materials Science and Engineering, Solid State Electronics, Uppsala University, Box 534, 75121 Uppsala, Sweden

† Electronic supplementary information (ESI) available. See https://doi.org/10.1039/d2ta01252a

such as durability, low cost and natural abundance of the catalyst materials.[4,5] Ni-based materials and layered hydroxides are recognized as promising electrocatalytic materials for water-splitting due to their relatively high catalytic activity, abundance, and low cost.[6–10] Layered double hydroxides (LDHs) are formulated as $[M_{1-x}^{2+}M_x^{3+}(OH)_2][A^{n-}]_{x/n}zH_2O$ and have a layered structure of divalent (M^{2+}) and trivalent (M^{3+}) metal cations bonded to hydroxides (OH^-) and inorganic or organic anions (A^{n-}) that compensate the charge, as well as neutral molecules (*i.e.*, H_2O).[11] NiFe LDH is known for its low overpotential and high current for OER.[7,8,12,13] The incorporation of Fe into Ni LDH enhances the catalytic properties, where one of the key underlying mechanisms for this is the improvement of the charge transfer kinetics between Ni^{2+} and Ni^{3+}.[14] In addition, the incorporation of iron also enhances the bi-functional capabilities of the NiFe LDH catalysts, allowing them to be used as both hydrogen and oxygen evolution reaction catalysts with improved activation after initial activation[13] and can provide advantages such as cost reduction and ease of production.

In addition, both the PV and electrolyzer components of a solar water-splitting device should be well-performing individually. It is also very important that the two parts are power matched. Finding an optimal operating current–potential point for the device plays a critical role in its overall performance.[15] To that point, a PV module comprised of cells that allow for an adjustable bandgap is a considerable advantage when seeking the optimal conditions for the solar water-splitting device for a designated catalyst system. $Cu(In,Ga)Se_2$ (CIGS) modules can be advantageous here since one can tune the bandgap of the CIGS cells by altering the Ga/(Ga + In) ratio to match the electrolysis requirement in a particular catalyst system across a range of temperatures and illumination intensity conditions.[16]

PV-electrolyzer device designs are important factors in the future implementation of solar water-splitting. Upscaling the system without diminishing the efficiency, however, is

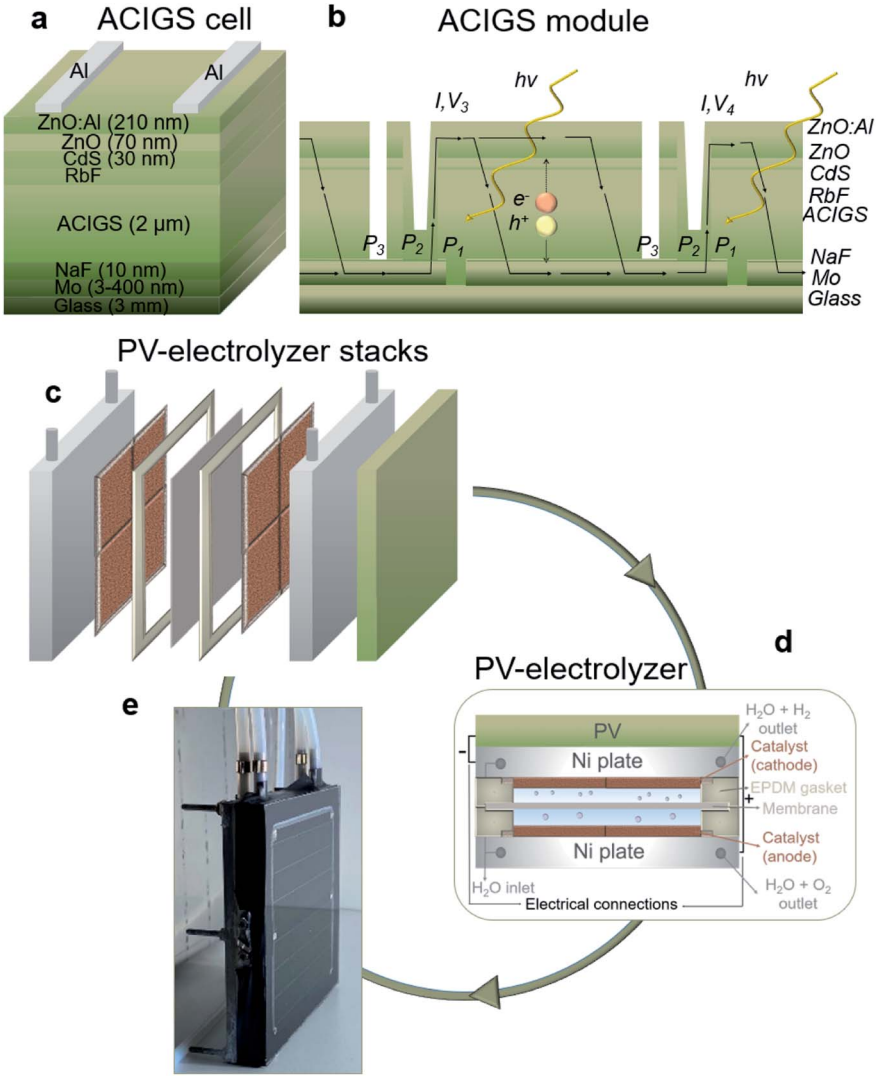

Fig. 1 Schematic images. (a) An ACIGS cell, (b) a monolithically-interconnected ACIGS multi-cell module (layers not at relative scale), (c) stacks, (d) device design, and (e) photograph of the integrated PV-electrolyzer for a combined ACIGS module and an NiFe LDH-based alkaline electrolyzer.

a challenge. Solutions arise in the form of a directly-coupled and thermally-contacted PV and electrolyzer system that can reduce grid-losses and those associated with DC–DC conversion, as well as enable a thermal exchange, which is beneficial for the total reaction by permitting the simultaneous cooling of the solar cells and heating of the electrolyzer.[17–19] Recently, we reported an 8.5–9.1% STH efficiency for a 100 cm^2 PV-electrolyzer consisting of a silver added CIGS (ACIGS) module and a thin film-based NiMoV (cathode) and NiO (anode) alkaline electrolyzer with a thermally-integrated design.[20] In this study, we developed a second generation of the thermally-integrated device using bifunctional NiFe LDH nanocatalysts combined with ACIGS modules. Material and functional properties of the developed catalyst and ACIGS modules are reported as well as the long-term indoor and outdoor hydrogen production performance of the integrated water splitting devices.

Results and discussion

PV characteristics of the synthesized and compiled ACIGS modules

Solar cell and contact materials were prepared with subsequent layer formation on glass with the structure; glass/Mo/NaF/ACIGS/CdS/ZnO/ZnO:Al/Al grid (Fig. 1a). Series interconnected cells on one monolithic substrate were obtained using a laser scribing step for the Mo layer (Fig. 1b). In this study, after synthesizing and depositing the layers, two ACIGS modules were developed with scribing using two cells consisting of three monolithically-interconnected cells: ACIGS-1 with 100.8 cm^2 and ACIGS-2 with 82.3 cm^2 total active areas. The modules were characterized under varying temperatures of between 25 and 55 °C with a constant irradiance of 100 mW cm^{-2}, as well as under varying irradiances of between 20 and 110 mW cm^{-2} at a constant temperature of 25 °C.

The PV characteristics of the ACIGS modules are specified in Fig. 2. The module efficiency decreased from 14.3 to 12.9%, and from 17.27 to 16.06% (Fig. 2a) for ACIGS-1 and ACIGS-2, at an elevation of temperature from 25 to 55 °C. This was an expected decrease, as it is known that elevated temperatures reduce PV performance,[17] but this is less discussed in the context of solar-driven or photoelectrochemical water-splitting. The fill factor (FF) for the synthesized materials and assembled modules was above 65.5% and stable with increasing temperatures for both modules (Fig. 2b). The open-circuit voltage (V_{OC}) of the ACIGS-2 module was slightly higher than that of the ACIGS-1 (with a 0.05–0.1 V difference) and decreased from 2.27 to 2.12 V, with the temperature increasing from 25 to 55 °C (Fig. 2c). The short

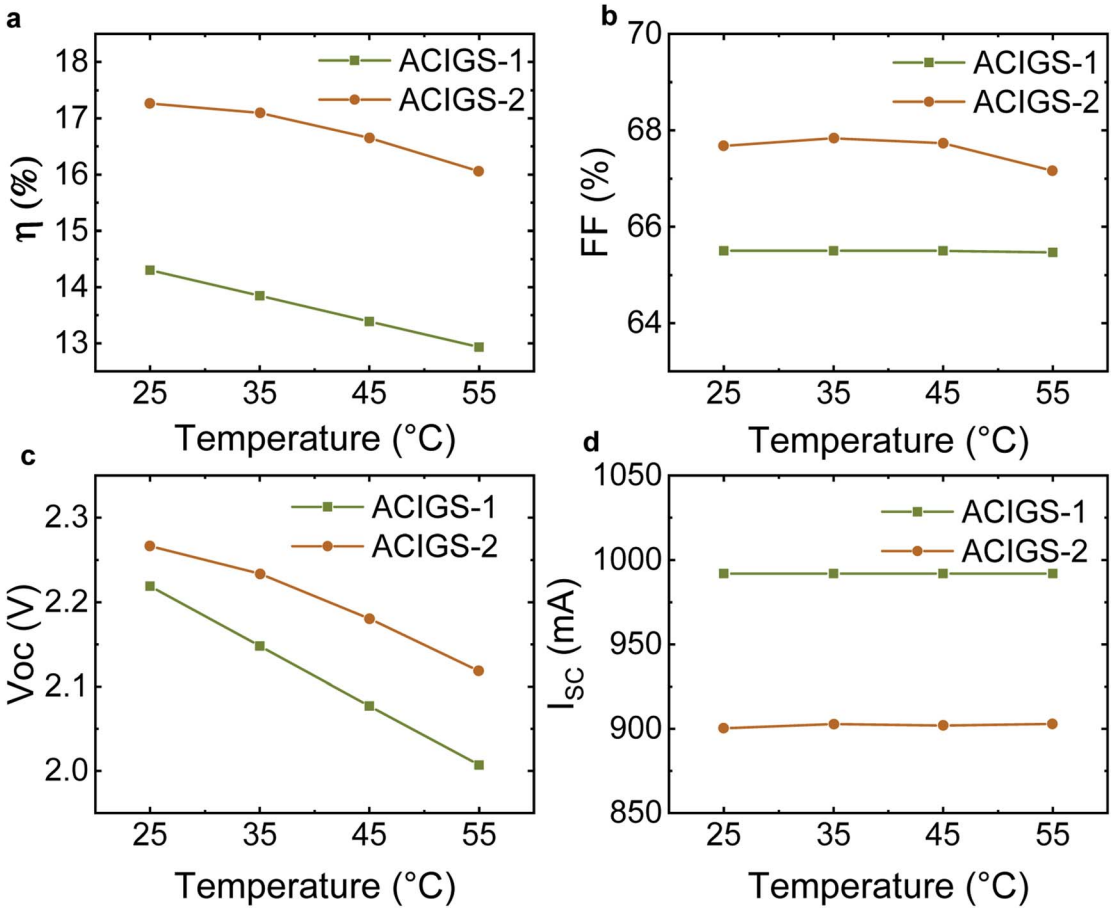

Fig. 2 PV module parameters for ACIGS-1 and ACIGS-2 modules a with 2 × 3-cell. (a) Module efficiency, (b) fill-factor (FF), (c) open-circuit voltage (V_{OC}), and (d) short-circuit current (I_{SC}). The illumination was AM1.5G with 100 mW cm^{-2}.

circuit currents (I_{SC}) were at 992 mA and 902 mA for ACIGS-1 and ACIGS-2, respectively, and were largely unaffected by varying the operating temperature from 25 to 55 °C (Fig. 2d).

Material properties and water-splitting performance of NiFe LDH

The NiFe LDH catalysts were prepared by means of a hydrothermal method. The catalyst surface morphology (Fig. 3a) and GIXRD pattern (Fig. 3b) of the hydrothermally-synthesized NiFe LDH catalysts were well-matched with previous works (Qiu *et al.*, 2019).[13] The Raman spectrum of the pristine catalyst is shown in Fig. 3c. The peak at 331 cm^{-1} can be assigned to the symmetric bending of the metal–oxygen bonds[21,22] in the material, whereas the peaks at 483 and 572 cm^{-1} are assigned to the F_{2g}(b) vibrations, with asymmetrical stretching of Fe–O and Ni–O bonds, and F_{2g}(c) vibrations and asymmetrical bending of the metal–oxygen bond, respectively.[21,22] The peaks at 699 and 1341 cm^{-1} correspond to the A_{1g} vibration, the symmetrical stretching of the Fe–O and Ni–O bonds, and the C–H bending, respectively.[21,22] Full peak assignments, together with comparable literature values, are presented in Table S1.†

The HER and OER performances of NiFe LDH catalysts were first evaluated by means of linear sweep voltammetry (LSV) in a three-electrode configuration. An overpotential of 262 mV for the HER and 212 mV for the OER were required to reach a current density of 10 mA cm^{-2} for the un-activated catalysts. One can note that in similarity with a previous study, the NiFe LDH catalyst show improved catalytic performance after activation and has been ascribed to enhanced crystallinity and increased surface area in a dynamic self-optimization during the activation.[9] Prior to building the thermally-integrated device for solar-driven water-splitting, the catalysts were activated in 1.0 M KOH by applying a current density corresponding to 10 mA cm^{-2} in a two-electrode configuration for 100 h at 25 °C. Following the activation, the overpotential for the HER (Fig. 3d) and OER (Fig. 3e) at 10 mA cm^{-2} decreased to 189 and 201 mV, respectively. A variety of *ex situ* techniques before and after activation together with operando Raman spectroscopy have

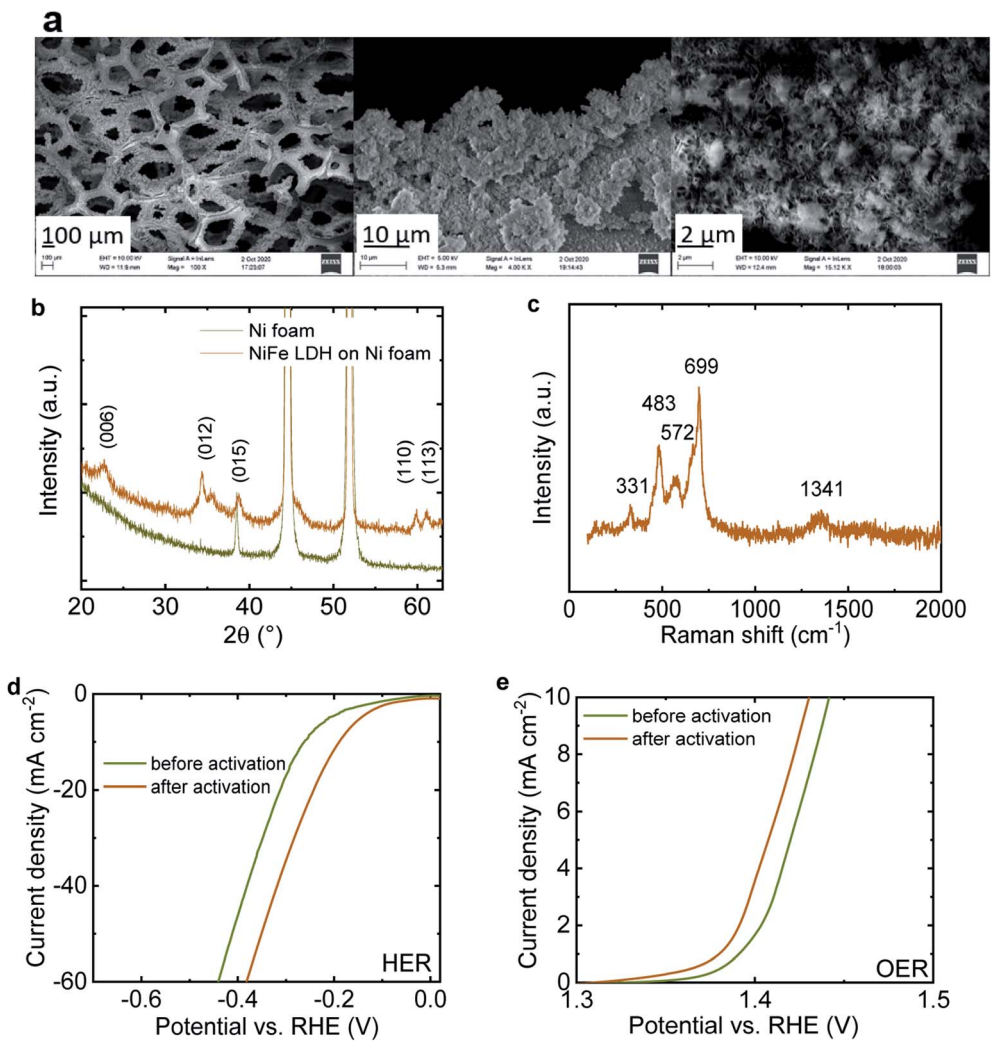

Fig. 3 Catalyst characterization of the NiFe LDH electrocatalysts. (a) SEM images, (b) XRD pattern, (c) Raman spectrum, (d) LSV measurements for HER, and (e) OER of the catalyst in 1 M KOH with a 5 mV s^{-1} scan rate.

previously been used to shown that the presence of Fe inhibit the Ni self-oxidation and promote water dissociation into H_2 under the HER process by formed FeOOH and complexation between adsorbed H and surface nickel cations, while γ-NiOOH and higher valence Ni was created during positive potential bias and the OER reaction.[13]

Thermally-integrated PV-electrolysis device design

Fig. 1c and d display the stack and device design of the solar-driven water-splitting device, and correspond to a closely-integrated PV-electrolyzer system that enables thermal exchange and minimizes ohmic losses. The integrated PV-electrolyzer device was formed by combining an encapsulated PV module with a low-gap-design electrolyzer using boron nitride thermal paste, the latter ensuring effective heat exchange from the solar cells to the catalyst system. The anodic and cathodic catalysts were designed to be closely connected to minimize mass transport limitations. A photo of the device is shown in Fig. 1e. An important but maybe not immediately apparent feature of the design is that it is built on stackable layers, including the contacts, where the device is assembled into a fully working system by just pressing them together with the electrolyzer part in the bottom. By this, there are several benefits. First, this allows a high throughput manufacturing by stamping out all layers except the PV-part. Second, the collection of modules into arrays can be simplified by having combined holders and pressure grids over the array. Third, by having the thin electrolyzer part in the bottom of the module in the design, the module can be building integrated as part of the wall or roof, enabling the use of the system also in climates that have water/electrolyte freezing conditions in the autumn-winter-spring. As with any complex system with a flow of liquids and potential malfunction of individual parts during the decades of use, the design allows for a convenient opening for service or replacement of parts during the lifetime of the device.

Current–voltage characteristics of the ACIGS modules and NiFe LDH-based electrolyzer

Current–voltage (*I–V*) measurements were performed for the alkaline NiFe LDH (cathode)-NiFe LDH (anode) electrolyzer at different temperatures between 25 and 55 °C and for the ACIGS modules (Fig. 4a and b). Tests at different irradiances were also conducted for the ACIGS-2 module at 25 °C (Fig. 4c). Operating potential and current, as well as preliminary STH efficiency, were calculated from the intersection point of the current–voltage curves of the ACIGS module and electrolyzer at the same temperatures. The STH efficiency calculation was made assuming 100% faradaic efficiency, while the final reported STH efficiency was instead extracted *via* characterization of the gas evolution.

The operating points of the ACIGS-1 electrolyzer corresponded to the maximum power point of the ACIGS-1 module and shifted to lower voltages and currents upon temperature increases (Fig. 4a), resulting in changes in the STH efficiency from 10 to 8.2% (Table 1).

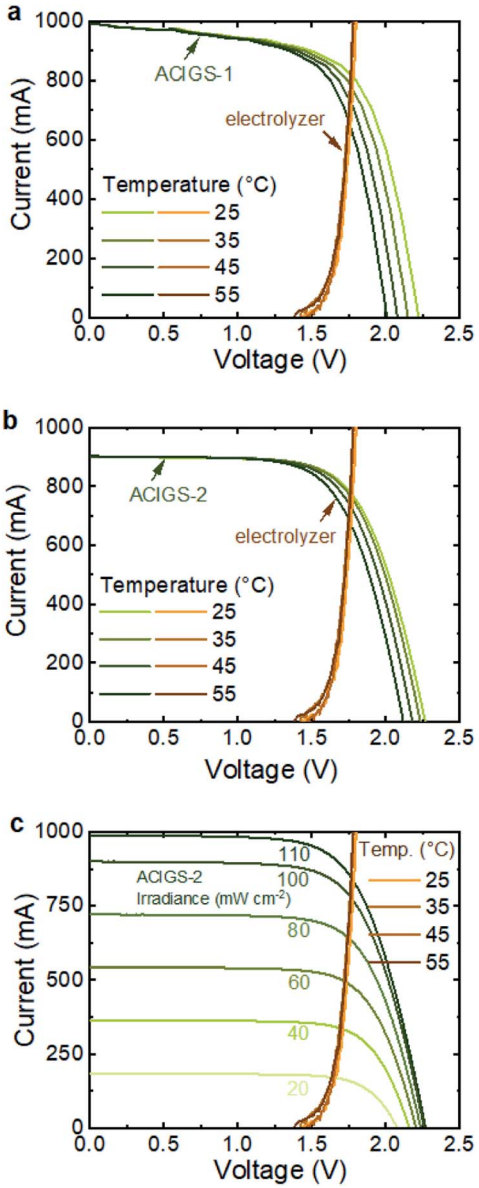

Fig. 4 Current–voltage (*I–V*) data of the PV module and electrolyzer parts. (a) Data for the electrolyzer and ACIGS-1 (100.8 cm^2), (b) ACIGS-2 (82.3 cm^2) modules consisting of 2 × 3 cells under 100 mW cm^{-2} irradiance and different temperatures, (c) *I–V* data for the ACIGS module under varying irradiances, as well as the electrolyzer. The electrolyzer is an alkaline NiFe LDH (cathode)-NiFe LDH (anode) model with a catalyst area of 100 cm^2.

The STH efficiency of the ACIGS-2 electrolyzer decreased from 11.6 to 10.3% with increasing temperature (Table 1), as the operating point corresponded to higher voltages on the right-hand side of the maximum power point and PV current changes drastically in this region (Fig. 4b). This calculation was performed to compare the experimental data of the PV and electrolyzer at the same temperature. On the other hand, temperature changes in the electrolyzer did not significantly affect the catalytic current compared to the temperature's effect on the PV data. Furthermore, as the catalyst load curve does not drastically change with the temperature *versus* the *I–V* curve of

Table 1 Operating potential (V_{int}), current (I_{int}), and STH efficiency from the intersection of the current–voltage curves of the ACIGS modules and alkaline NiFe LDH (cathode)-NiFe LDH (anode) electrolyzer

Module	Irradiance (mW cm^{-2})	T (°C)	V_{int} (V)	I_{int} (mA)	STH (%)
ACIGS-1	100	25	1.78	809	10.0
		35	1.76	786	9.7
		45	1.76	733	9.0
		55	1.74	669	8.2
ACIGS-2	100	25	1.77	772	11.6
		35	1.76	766	11.5
		45	1.75	739	11.1
		55	1.75	690	10.3
ACIGS-2	110		1.78	834	11.4
	100		1.77	771	11.6
	80		1.76	639	12.0
	60		1.74	488	12.2
	40		1.71	335	12.6
	20		1.66	170	12.7

the PV, no strong temperature dependence can be seen in Fig. 4. The results thus indicate that one would not expect a noteworthy difference in STH efficiency. For instance, if the PV temperature is 55 °C and the electrolyzer temperature is any temperature between 25 and 55 °C, the STH efficiency only changes from 10.1 to 10.3%.

In the irradiance response test conducted for ACIGS-2, the STH efficiency was seen to increase from 11.4 to 12.7% with decreasing irradiance (Table 1). This behaviour arises from the lower required overpotential at lower catalytic currents and a more optimally-placed catalyst load curve with respect to the ACIGS-2 module *I–V* curve (Fig. 4c). However, as hydrogen production is proportional to the current, one should expect a lower amount of hydrogen at lower irradiances, *e.g.*, the catalytic current decreased from 834 to 170 mA when the irradiance decreased from 110 to 20 mW cm^{-2}.

Hydrogen production performance of the ACIGS-1 electrolyzer

A continuous hydrogen evolution measurement was performed for the ACIGS-1 PV-electrolyzer device under 100 mW cm^{-2} illumination provided by a class-A solar spectrum lamp (Plasma-I AS1300 from Plasma International) for seven days (168 hours). A schematic illustration of the whole setup for the gas volume measurement is shown in Fig. 5a. The electrolyte (1 M KOH, pH = 14) fed the anodic and cathodic sides from two containers (polypropylene, 1 L) through Teflon tubes at a flow rate of 50 ml min^{-1}. An inverted graduated cylinder was used for the gas volume measurement.

The hydrogen production rate for the seven-day measurement (Fig. 5b) was 5.4 ml min^{-1} on average, with an almost stable trend over time. The voltage (Fig. 5c) and current (Fig. 5d) were also recorded during gas measurements, revealing that more than 1.7 V and 700 mA were necessary to drive the water-splitting reaction. The maximum STH efficiency reached 10%, whereas the electricity-to-hydrogen (ETH) efficiencies were 75–80% (Fig. 5e), and the average STH efficiency was 9.7% (Fig. 5f). During the measurements, the temperatures of the ACIGS-1 module, electrolyzer, electrolyte, and ambient were monitored and are shown in Fig. 5g and with extracted average temperatures of 54, 48, 39, and 37 °C, respectively. A demonstration video of the scalable, thermally-integrated ACIGS-1 alkaline electrolysis device can be found in the ESI.† Although we here present one up-scaled unit, it can conveniently be assembled into an array of devices with mutual gas-handling in similarity to the larger PV modules found in conventional solar cell technology.

Hydrogen production performance of the ACIGS-2 electrolyzer

STH efficiency *via* gas evolution and thus the hydrogen production of the ACIGS-2-electrolyzer were investigated under laboratory conditions prior to investigating the outdoor performance of the device, which was illuminated with a continuous wave sun simulator (AM 1.5G spectrum; 100 mW cm^{-2}, 25 °C, class AAA), with the generated hydrogen kept in an inverted burette bell. The changes in the fluid level were manually monitored over time. At the start of the measurement, the STH efficiency was 8.5% but remained above 10% for the remainder of an eleven-hour measurement at 100 mW cm^{-2} (ESI Fig. 1a†). The STH values obtained from the hydrogen production agreed with those calculated from the *I–V* data. The maximum STH efficiency from the gas volume measurement was 13.4% (even higher than the STH derived from the current–voltage intersection between the PV and electrolyzer), showing that the device design featured very low mass transport losses and a faradaic efficiency close to unity. It also highlights that the NiFe LDH catalyst becomes dynamically self-optimized and improves over time, as previously reported.[13] The average STH efficiency was 11.3%, with the corresponding average hydrogen production rate of 5.74 ml min^{-1} (ESI Fig. 1b†) and an area-specific hydrogen production rate of 3.74 g h^{-1} m^{-2}.

PV-electrolysis outdoor performance of the ACIGS-2 alkaline electrolyzer with a NiFe LDH electrocatalyst

The thermally-integrated ACIGS-2 module and NiFe LDH-based alkaline electrolyzer system was placed at the installation site (Fig. 6a) in Jülich, Germany (55° 55′ N; 6° 21′ E) in December of 2020 and hydrogen production was recorded for a 21 day outdoor test. The test location, a framework with a southern orientation and an angle of 35° to the horizontal, was built on a laboratory rooftop. To measure the hydrogen gas flow, a stainless-steel vessel was filled with water at the beginning. During the operation, the water was repressed from the hydrogen, and the total volume of the repressed water was measured at the end of a day representing the total hydrogen evolution. Additionally, a box with a drying agent and a mass flow meter was integrated into the hydrogen outlet, indicating the change in flow rate over the time period. In order to calculate the energy balances, a pyranometer (Kipp & Zonen) was also mounted in the same orientation as the thermally-integrated device.

The data on irradiation from the 21 days of measurement and corresponding STH efficiency are presented in Fig. 6b and

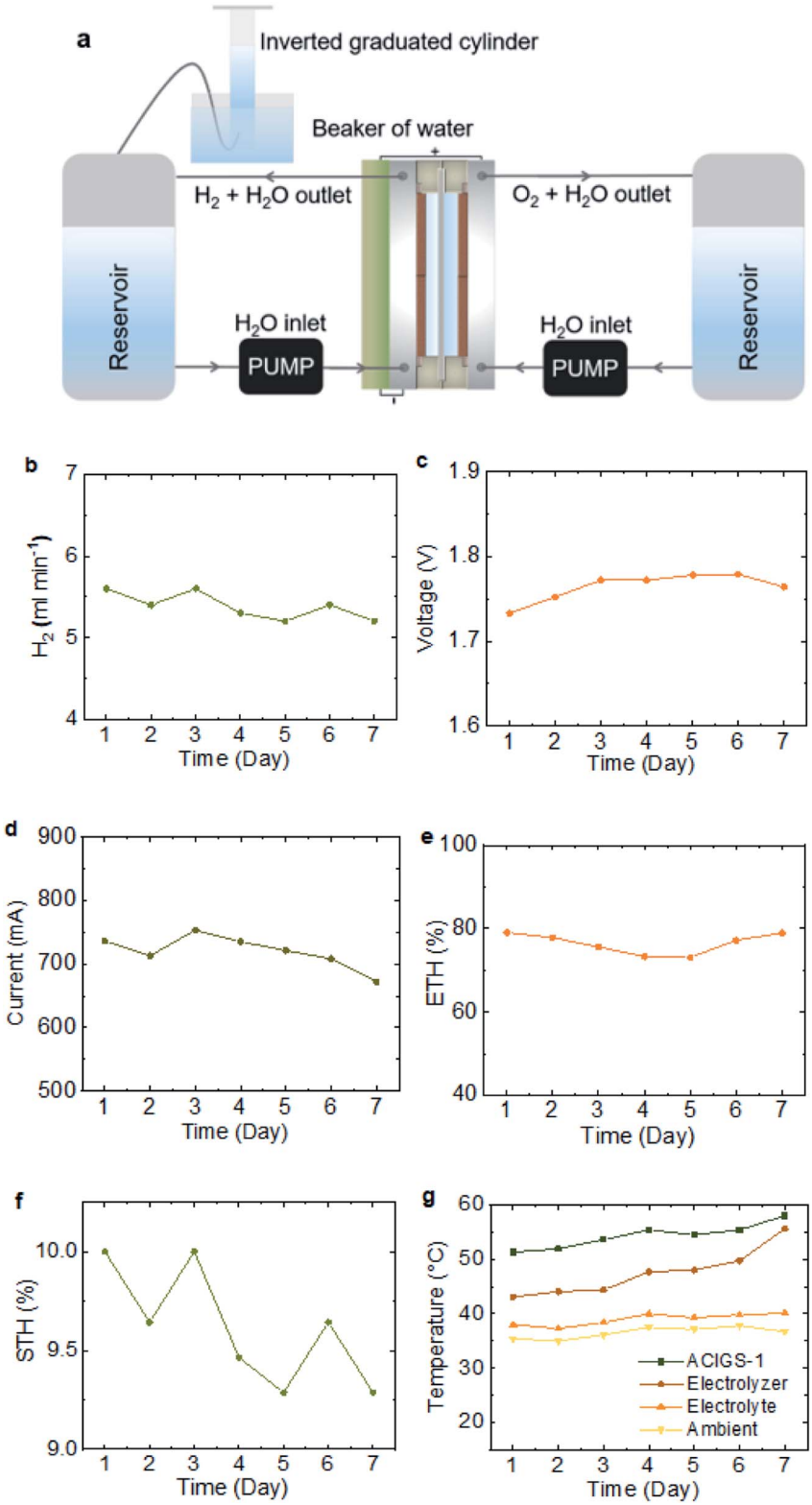

Fig. 5 Seven-day (168 hours) indoor performance of the PV-electrolyzer. (a) Schematic illustration of the full setup for the integrated 2 × 3-cell ACIGS-1 module alkaline electrolyzer of the NiFe LDH (cathode)-NiFe LDH (anode) device, (b) hydrogen production, (c) voltage at the operation point, (d) current at the operation point, (e) ETH efficiency, (f) STH efficiency, and (g) temperatures of the PV module, electrolyzer, electrolyte, and ambient. The PV-electrolyzer featured an integrated 100.8 cm^2 ACIGS-1 module and NiFe LDH (cathode)-NiFe LDH (anode) for electrolysis with a 100 cm^2 area. The illumination was 100 mW cm^{-2}.

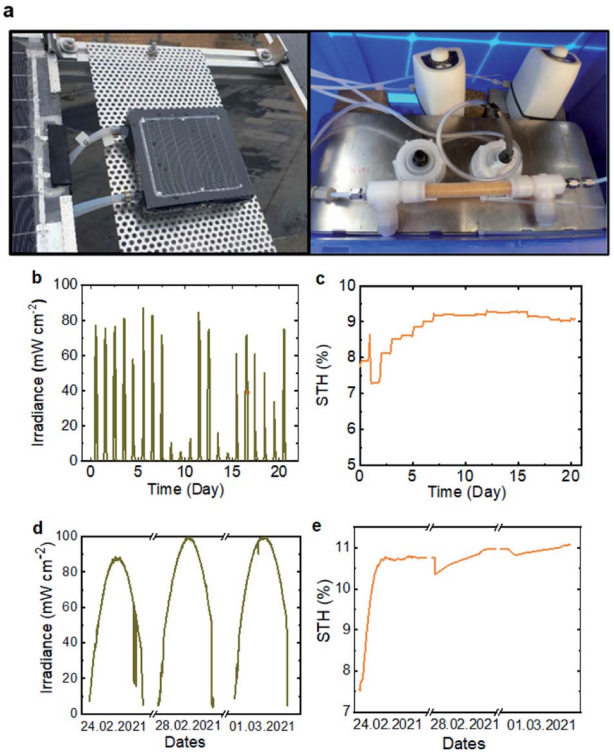

Fig. 6 Outdoor performance of the PV-electrolyzer. (a) Photos of the PV-electrolyzer setup at the installation site in Jülich, Germany (55° 55′ N, 6° 21′ E), (b) irradiance, (c) STH at ambient temperature for the 21 day (500 hour)-measurement, (d) irradiance, and (e) STH for for the hourly outdoor measurement in "clear sky" on 24/02, 28/02 and 01/03/2021. The PV-electrolyzer comprised the integrated 2 × 3 cell ACIGS-2 module with a total area of 82.3 cm^2 ACIGS-2 module-alkaline electrolyzer NiFe LDH (cathode)-NiFe LDH (anode) with a 100 cm^2 catalyst area. The electrolyte was 1 M KOH.

c, respectively. The ambient temperature and hourly measurement of the produced hydrogen are shown in ESI Fig. 2a and b,† respectively. The weather was cloudier and colder during the 21 day measurement. Therefore, a three-day measurement was performed when much warmer weather and a clear sky occurred (Fig. 6d). Although the temperature and intensity of the sun were relatively low, the system ran well, and the STH efficiency was in the range of 10% (Fig. 6d), with a 3.34 g h^{-1} m^{-2} area-specific hydrogen production rate.

Comparison with the literature

An STH efficiency of 10% has previously been achieved by CIGS-based water electrolysis at the lab-scale using precious catalysts[23,24] using solar cell modules with about 17% efficiency. The catalysts for both the HER and OER were platinum black deposited on 4 cm^{-2} platinum foils, and the electrolyte was 3 M H_2SO_4 (pH = 0). A key method here was to employ a device of serially-interconnected cells,[24] instead of the more expensive and challenging approach entailed by using tandem devices. The theoretical maximum for PV-driven water-splitting at a relatively high rate, using a tandem device and

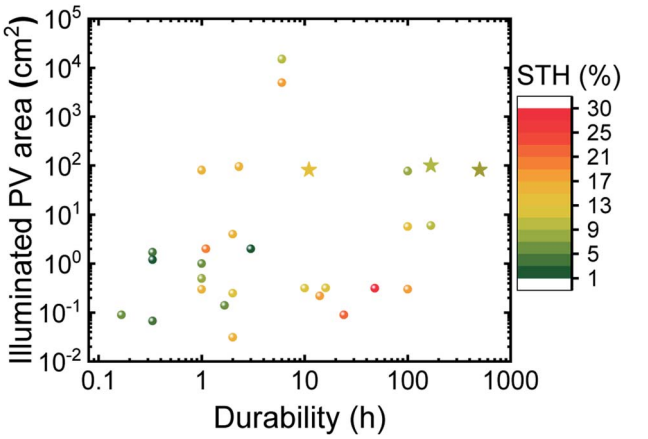

Fig. 7 The scalability, stability, and STH efficiency of PV-electrolysis systems. Comparison of the STH efficiency, stability and scalability for the reported integrated CIGS PV-alkaline electrolyzers with various results of studies of PV-electrolysis systems in the literature. The star symbols represent the results of this work. Details and the system references are presented in Table 2.

optical absorption limit, is 32%, whereas a serially-interconnected device is expected to be close to 25% STH.[25] However, given the much more cost-effective serial interconnection approach (which bypasses the need for transparent inter-layers and detailed spectral matching, as in tandem devices), a greater interest in this approach has also become apparent since the three-cell serial interconnected CIGS approach with 10% STH in 2013,[24] 10% STH reported for four serially-interconnected Si-cells,[34] 12.3% STH for a two-cell perovskite-based device,[52] and 7.7% STH for serially-interconnected triple-junction Si-based device[53] for smaller lab-scale devices. In a recent work, climate modelling was performed using current–voltage data from the laboratory measurements of larger devices using CIGS, several Si-modules (crystalline Si, Si heterojunction, and thin-film Si), and a thin film-based alkaline electrolyzer.[17] The performance of the thermally-connected PV-electrolyzer was investigated using the climatic data of Jülich, Germany, with a one-hour resolution for an entire year. The average annual STH efficiency was calculated as 11% for a 10 m^2 NiMoW–NiO electrolyzer and a three-cell CIGS of the same size. An STH efficiency of above 12% was achieved for a lab-scale module, whereas 8.5% was obtained experimentally for the modeled device of the same size as that discussed in this study, underlining the challenges of retaining high efficiencies in larger modules.[20]

The performance of various solar water-splitting systems was reviewed in 2015 by Ager *et al.*,[54] in 2019 by Kim *et al.*,[55] and by Tembhurne *et al.*[48] Fig. 7 graphically depicted the performance of various PV-electrolysis systems in terms of STH efficiency, stability, and scalability. Further details of these are listed in Table 2. The results show that in terms of performance, our integrated PV-electrolyzer is amongst the largest integrated

Table 2 Comparison of PV-electrolysis systems

	PV				Electrolyzer					PV-electrolyzer performance		
Irradiation (Sun)	PV type	PCE (%)	PV area (cm^2)	PV cell number	Cathode material	Anode material	Catalyst area (cm^2)	Electrolyte	Membrane	STH (%)	Durability (h)	Ref.
1	2 np GaAs		1 (n) to 4 (p)		Ti/RuO_2	Pt foil	4 (C) to 1 (A)	5 M H_2SO_4		8.00		1984, Murphy *et al.*[26]
135	AlGaAs on Si		0.22	1	RuO_2 on Ti foil	Pt black on Pt mesh	10	1 M $HClO_4$	Not used	18.30	14.00	2000, Licht *et al.*[27]
1	GaInP/GaAs	28.5	0.3	1	Pt foil	Pt foil	0.3	2 M KOH	Not used	16.50	1.00	2001, Khaselev *et al.*[28]
1	Triple p–i–n a-Si	9	0.5	3	Pt foil	Pt foil	0.5	2 M KOH	Not used	7.80	1.00	2001, Khaselev *et al.*[28]
500	$Ga_{0.35}In_{0.65}P$–$Ga_{0.83}In_{0.17}As$ double junction	19.6	96	6	Pt	Ir	30	Polymer electrolyte	PEM	15.10	2.30	2007, Peharz *et al.*[29]
97	c-Si single junction	14.2	13 010	72	Pt on carbon	IrO_2 or RuO_2	100 (20 cell)		Nafion	12.40		2008, Gibson *et al.*[30]
1	a-Si triple junction	6.2	2		NiMoZn	Co	2	1 M KBi	Not used	2.50	3.00	2011, Reece *et al.*[31]
1	CIGS	17	3	3	Pt black on Pt foil	Pt black on Pt foil	4	3 M H_2SO_4		10.50	27	2013, Jacobsson *et al.*[24]
10.2	GaInP/GaAs/Ge three-tandem cell		1	2	Pt loaded carbon paper	Pt loaded carbon paper	4 (4 cells)	Water		6.10	1.00	2013, Fujii *et al.*[32]
0.49	c-Si		81.2	4	Pt loaded carbon paper	Pt loaded carbon paper	5 (4 cells)	Water		15.30	1.00	2013, Fujii *et al.*[32]
1	$CH_3NH_3PbI_3$ tandem	15.7	0.318	2	NiFe LDH	NiFe LDH	5	1 M NaOH	Not used	12.30	10.00	2014, Luo *et al.*[33]
1	c-Si single junction	16	6	4	NiMoZn	NiBi		0.5 M KBi	Not used	10.00	168.00	2014, Cox *et al.*[34]
724	III–V multijunction		0.0314	3	Ti	Ti	1.13	Water	PEM	16.80	2.00	2014, Rau *et al.*[35]
1	GaInP/GaAs/Ge	38	0.09		Ni foam	Ni foam	10	1 M KOH	Not used	22.40	24.00	2015, Bonke *et al.*[36]
1	Triple junction organic	6.7	0.0676		Ti/RuO_2	Ti/RuO_2	1.1 (A) to 1.2 (C)	1 M KOH		5.40	0.33	2015, Esiner *et al.*[37]
1	Triple junction organic	6.5	0.0676		NiMoZn	Co_3O_4		0.1 KBi		4.90	0.33	2015, Esiner *et al.*[37]
1	Triple junction organic	6.1	1.7		Ti/RuO_2	Ti/RuO_2	1.2	1 M KOH		3.60	0.33	2015, Esiner *et al.*[37]
1	Triple junction organic		1.2		NiMoZn on NiFoil	Co_3O_4 on ITO		0.1 KBi		1.30	0.33	2015, Esiner *et al.*[37]

Table 2 (*Contd.*)

	PV				Electrolyzer					PV-electrolyzer performance		
Irradiation (Sun)	PV type	PCE (%)	PV area (cm^2)	PV cell number	Cathode material	Anode material	Catalyst area (cm^2)	Electrolyte	Membrane	STH (%)	Durability (h)	Ref.
800	Triple junction	24	400	3 series 1 parallel	Pt loaded carbon paper	Pt loaded carbon paper	(4 series 3 parallel electrolyzer)	Water	PEM	17.10		[a]2015, Sugiyama *et al.*[38]
761.2	InGaP/GaAs/Ge	31.2	0.057	3	Pt loaded carbon paper	Pt loaded carbon paper	48 (5 cells)	Water	PEM	24.40		2015, Nakamura *et al.*[39]
1	Bifacial heterojunction c-Si		5.7	3	Pt	IrO_x	1.3	1 M KOH	Nafion	14.20	100.00	2016, Schüttauf *et al.*[40]
420	InGaP/GaAs/GaInNAsSb triple junction	39	0.316		Pt black	Ir black	6.25 (2 cell)	Nafion 117	Nafion	30.00	48.00	2016, Jia *et al.*[41]
1	PBDTTPD and the fullerene acceptor PC PBDTTPD: PCBM homo-tandem	8.35	0.1		Pt	Ni		1 M NaOH		6.00		2016, Gao *et al.*[42]
1	$FAPbI_3$-$MAPbBr_3$		0.32	2	CoP on Ti foil	NiFe LDH	2.27	0.5 M H_2SO_4 (C) to 1 M KOH (A)	Bipolar membrane	12.70	16.00	2016, Luo *et al.*[43]
500	DSSC tandem 2p, 4 terminal	12.3	0.141	2	Pt	Pt	0.066	1.0 M NaOH	Not used	5.75	1.67	2017, Kang *et al.*[44]
1	Lead halide perovskite	14.69	0.25	2	NiP	$Na_{0.08}Ni_{0.9}Fe_{0.1O2}$ LDH	1	1 M KOH		11.22	2.00	2017, Weng *et al.*[45]
1	Single junction GaAs	26.5	2	2	Pt/C on carbon fiber paper	IrO_x on carbon fiber paper	6		Nafion	20.60	1.10	[a]2017, Chang *et al.*[46]
1	Single III–V triple junction	32.6	0.3025		NiMoS on C cloth	MHCM-z-BCC on carbon cloth	1	0.5 mol Na_2HPO_4 sea water	Not used	17.90	100.00	2018, Hsu *et al.*[47]
474	InGaP-InGaAs-Ge	39	4	4	Pt	$IrRuO_x$	25	Water	Nafion	15.00	2.00	2019, Tembhurne *et al.*[48]
750	Concentrated PV		5000	2	Pt	Ir	(14 cell)	Water		18.70	6.00	2020, Bashir *et al.*[49]
1	Si		15 000	1	Pt	Ir	(17 cell)	Water		9.40	6.00	2020, Bashir *et al.*[49]
1	$MAPbI_3$ perovskite	10.6	0.09	2	CoP on FTO	CoP on FTO	0.09	1 M KOH	Not used	6.70	0.17	2020, Liang *et al.*[50]
1	$MAPbBr_xI_{(3-x)}$ perovskite	18.9	0.5	2	MoS_2 on C paper	NiFe on C paper	0.5	1 M KOH		From 12.67 to 5.78	17	2021, Asiri *et al.*[51]
1	$(Ag,Cu)(In,Ga)Se_2$	16	78	4	NiMoV on Ni foam	NiO	100	1 M KOH	AEM	8.50	100.00	2021, Pehlivan *et al.*[20]

Table 2 (*Contd.*)

PV					Electrolyzer					PV-electrolyzer performance		
Irradiation (Sun)	PV type	PCE (%)	PV area (cm^2)	PV cell number	Cathode material	Anode material	Catalyst area (cm^2)	Electrolyte	Membrane	STH (%)	Durability (h)	Ref.
1	(Ag,Cu)(In,Ga)Se_2	14.3	100.8	2 × 3	NiFe LDH on Ni foam	NiFe LDH on Ni foam	100	1 M KOH	AEM	9.70	168.00	This work
1	(Ag,Cu)(In,Ga)Se_2	17.27	82.3	2 × 3	NiFe LDH on Ni foam	NiFe LDH on Ni foam	100	1 M KOH	AEM	11.30	11.00	This work
1	(Ag,Cu)(In,Ga)Se_2	17.27	82.3	2 × 3	NiFe LDH on Ni foam	NiFe LDH on Ni foam	100	1 M KOH	AEM	13.40	After 7 h	This work
<0.8	(Ag,Cu)(In,Ga)Se_2	17.27	82.3	2 × 3	NiFe LDH on Ni foam	NiFe LDH on Ni foam	100	1 M KOH	AEM	10–11	500.00	This work-outdoor test

[a] Has DC–DC converter; AEM: anion exchange membrane; a-Si: amorphous silicon; c-Si: crystalline silicon; DSSC: dye-sensitized solar cell.

devices with high levels of efficiency and stability, and it offers promising scalability.

Conclusions and final remarks

In this study, thermally-integrated PV-alkaline electrolysis modules were developed using NiFe LDH nanocatalysts with 82–100 cm^2 areas and six-cell ACIGS modules. SEM, GIXRD, and Raman spectroscopy measurements were performed to characterize the material properties of the catalyst, as well as electrochemical measurements of the catalytic properties. *I–V* measurements were also performed for the electrolyzer and PV module.

The PV-electrolysis system was designed in such a way that the electrolysis module can work as a cooling system for the PV module. This is beneficial due to the fact that PV efficiency is higher at lower operating temperatures, and electrolysis efficiency increases at higher temperatures. The STH efficiency was determined with both *I–V* or gas volume measurements. We achieved 10 and 9.7% maximum and average STH efficiencies for a seven-day measurement, respectively, corresponding to a 5.4 ml min^{-1} average hydrogen production rate and a 2.87 g h^{-1} m^{-2} area-specific hydrogen production rate for a six-cell ACIGS module with 14.3% efficiency integrated into a NiFe LDH catalyst-based electrolyzer in which the catalysts and PV module had areas of 100 cm^2. The same nanocatalyst-electrolyzer, with a 100 cm^2 area, was combined with a six-cell ACIGS module with an active area of 82.3 cm^2 and a 17.27% module efficiency under 100 mW cm^{-2} illumination. We obtained a 13.4% maximum STH efficiency from the gas volume measurement under 100 mW cm^{-2} irradiance for this system. The average STH efficiency was 11.3%, with the corresponding 5.74 ml min^{-1} hydrogen production rate and area-specific hydrogen production rate of 3.74 g h^{-1} m^{-2}. The thermally-integrated device for the outdoor test was erected in Jülich, Germany, in December 2020 and resulted in an STH efficiency in the range of 10% under unfavourable weather conditions for the tests.

The device design with the electrolyzer part in the bottom allows for potential building integration with the added benefit of the possibility to use the system also in climates with freezing conditions for the electrolyte during winter. Furthermore, the stackable layers assembled into the device using only pressure allow for simplified assembly and de-assembly for convenient maintenance during the lifetime of the module or array of modules. Although the approach utilizes excess heat otherwise lost and has among the highest reported STH efficiencies for integrated devices and promising stability, several remaining challenges remain. These are related to the competition with conventional PV-electrolysis. The latter has the advantage of naturally being compatible with building integration, placing the electrolyzer indoors in colder climates, and composed of individual parts for easy maintenance compared to integrated solutions.[56] The present design circumvent some of these shortcomings for photoelectrochemical or integrated PV-electrolyzer system, but the conventional PV-electrolyzer system has the additional advantage of a larger freedom in

the form and where to place the electrolyzer. The latter also has the benefit of more flexible use of other renewable energy sources, such as wind- or hydropower, to run the electrolyzer when there is no sunlight, and also to use the electricity directly if there is no need for storage into a solar fuel. Irrespectively of these challenges, which exist in most photoelectrochemical or integrated devices for solar water splitting systems compared to PV-electrolysis, the results show thin-film PV materials and earth-abundant electrocatalysts can obtain very promising STH efficiencies at high hydrogen production rate in up-scaled modules for un-assisted solar-driven water splitting.

Author contributions

I. B. P., N. A. S., and Z. Q. contributed to the catalyst preparation. I. B. P. and N. A. S. performed catalyst characterization and analyzed the data. I. B. P. and J. O. performed the device measurements. I. B. P., M. E., L. S., and T. E. contributed to the device design and implementation of the research, as well as the analysis of the results. Indoor and outdoor tests in Julich were conducted by M. L. and W. Z. and directed by S. H. and M. M., I. B. P and T. E. wrote the first draft of the manuscript. All authors discussed the results and commented on the final manuscript. T. E. designed and directed the project.

Conflicts of interest

The authors have no competing interests to disclose.

Acknowledgements

We gratefully acknowledge the financial support for the "PEC-SYS" project, which has received funding from the Fuel Cells and Hydrogen 2 Joint Undertaking under grant agreement No. 735218, supported by the European Union (Horizon 2020), Hydrogen Europe, and N. ERGHY. J. The authors would like to thank Johan Mathiasson, Kathrin Theelen, Peter Neretnieks, and Johan Endrell for discussions and Christoph Zahren for supporting the measurements. This work was also supported by the Swedish Research Council (2015-03814).

References

1 A. Grimm, W. A. de Jong and G. J. Kramer, *Int. J. Hydrogen Energy*, 2020, **45**, 22545–22555.
2 R. L. LeRoy, *Int. J. Hydrogen Energy*, 1983, **8**, 401–417.
3 P. Haug, B. Kreitz, M. Koj and T. Turek, *Int. J. Hydrogen Energy*, 2017, **42**, 15689–15707.
4 W. Liu, F. Wen and Y. Xue, *J. Mod. Power Syst. Clean Energy*, 2017, **5**, 439–450.
5 M. Götz, J. Lefebvre, F. Mörs, A. McDaniel Koch, F. Graf, S. Bajohr, R. Reimert and T. Kolb, *Renewable Energy*, 2016, **85**, 1371–1390.
6 C. Fan, D. L. Piron, A. Sleb and P. Paradis, *J. Electrochem. Soc.*, 1994, **141**, 382–387.
7 P. M. Bodhankar, P. B. Sarawade, G. Singh, A. Vinu and D. S. Dhawale, *J. Mater. Chem. A*, 2021, **9**, 3180–3208.
8 L. Lv, Z. Yang, K. Chen, C. Wang and Y. Xiong, *Adv. Energy Mater.*, 2019, **9**, 1803358.
9 C. Feng, M. B. Faheem, J. Fu, Y. Xiao, C. Li and Y. Li, *ACS Catal.*, 2020, **10**, 4019–4047.
10 X. Li, C. Liu, Z. Fang, L. Xu, C. Lu and W. Hou, *Small*, 2022, **18**, 2104354.
11 Q. Wang and D. O'Hare, *Chem. Rev.*, 2012, **112**, 4124–4155.
12 M. Gong, Y. Li, H. Wang, Y. Liang, J. Z. Wu, J. Zhou, J. Wang, T. Regier, F. Wei and H. Dai, *J. Am. Chem. Soc.*, 2013, **135**, 8452–8455.
13 Z. Qiu, C.-W. Tai, G. A. Niklasson and T. Edvinsson, *Energy Environ. Sci.*, 2019, **12**, 572–581.
14 D. Yue, X. Yan, C. Guo, X. Qian and Y. Zhao, *J. Phys. Chem. Lett.*, 2020, **11**, 968–973.
15 M. Müller, W. Zwaygardt, E. Rauls, M. Hehemann, S. Haas, L. Stolt, H. Janssen and M. Carmo, *Energies*, 2019, **12**, 4150.
16 İ. Bayrak Pehlivan, M. Edoff, L. Stolt and T. Edvinsson, *Energies*, 2019, **12**, 4064.
17 İ. Bayrak Pehlivan, U. Malm, P. Neretnieks, A. Glüsen, M. Müller, K. Welter, S. Haas, S. Calnan, A. Canino, R. G. Milazzo, S. M. S. Privitera, S. Lombardo, L. Stolt, M. Edoff and T. Edvinsson, *Sustainable Energy Fuels*, 2020, **4**, 6011–6022.
18 S. Kirner, P. Bogdanoff, B. Stannowski, R. van de Krol, B. Rech and R. Schlatmann, *Int. J. Hydrogen Energy*, 2016, **41**, 20823–20831.
19 K. Welter, V. Smirnov, J.-P. Becker, P. Borowski, S. Hoch, A. Maljusch, W. Jaegermann and F. Finger, *ChemElectroChem*, 2017, **4**, 2099–2108.
20 İ. B. Pehlivan, J. Oscarsson, Z. Qiu, L. Stolt, M. Edoff and T. Edvinsson, *iScience*, 2021, **24**, 101910.
21 N. Dalai, B. Mohanty, A. Mitra and B. Jena, *ChemistrySelect*, 2019, **4**, 7791–7796.
22 K. Virkler and I. K. Lednev, *Forensic Sci. Int.*, 2008, **181**, e1–5.
23 T. J. Jacobsson, C. Platzer-Björkman, M. Edoff and T. Edvinsson, *Int. J. Hydrogen Energy*, 2013, **38**, 15027–15035.
24 T. J. Jacobsson, V. Fjällström, M. Sahlberg, M. Edoff and T. Edvinsson, *Energy Environ. Sci.*, 2013, **6**, 3676–3683.
25 T. J. Jacobsson, V. Fjällström, M. Edoff and T. Edvinsson, *Sol. Energy Mater. Sol. Cells*, 2015, **134**, 185–193.
26 O. Murphy and J. Bockris, *Int. J. Hydrogen Energy*, 1984, **9**, 557–561.
27 S. Licht, B. Wang, S. Mukerji, T. Soga, M. Umeno and H. Tributsch, *J. Phys. Chem. B*, 2000, **104**, 8920–8924.
28 O. Khaselev, A. Bansal and J. A. Turner, *Int. J. Hydrogen Energy*, 2001, **26**, 127–132.
29 G. Peharz, F. Dimroth and U. Wittstadt, *Int. J. Hydrogen Energy*, 2007, **32**, 3248–3252.
30 T. L. Gibson and N. A. Kelly, *Int. J. Hydrogen Energy*, 2008, **33**, 5931–5940.
31 S. Y. Reece, J. A. Hamel, K. Sung, T. D. Jarvi, A. J. Esswein, J. J. H. Pijpers and D. G. Nocera, *Science*, 2011, **334**, 645–648.
32 K. Fujii, S. Nakamura, M. Sugiyama, K. Watanabe, B. Bagheri and Y. Nakano, *Int. J. Hydrogen Energy*, 2013, **38**, 14424–14432.

33 J. Luo, J.-H. Im, M. T. Mayer, M. Schreier, M. K. Nazeeruddin, N.-G. Park, S. D. Tilley, H. J. Fan and M. Grätzel, *Science*, 2014, **345**, 1593–1596.
34 C. R. Cox, J. Z. Lee, D. G. Nocera and T. Buonassisi, *Proc. Natl. Acad. Sci. U. S. A.*, 2014, **111**, 14057–14061.
35 S. Rau, S. Vierrath, J. Ohlmann, A. Fallisch, D. Lackner, F. Dimroth and T. Smolinka, *Energy Technol.*, 2014, **2**, 43–53.
36 S. A. Bonke, M. Wiechen, D. R. MacFarlane and L. Spiccia, *Energy Environ. Sci.*, 2015, **8**, 2791–2796.
37 S. Esiner, R. E. M. Willems, A. Furlan, W. Li, M. M. Wienk and R. A. J. Janssen, *J. Mater. Chem. A*, 2015, **3**, 23936–23945.
38 M. Sugiyama, A. Nakamura, K. Watanabe, Y. Ota, K. Nishioka, Y. Nakano and K. Fujii, in *2015 IEEE 42nd Photovoltaic Specialist Conference (PVSC)*, IEEE, New Orleans, LA, 2015, pp. 1–4.
39 A. Nakamura, Y. Ota, K. Koike, Y. Hidaka, K. Nishioka, M. Sugiyama and K. Fujii, *Appl. Phys. Express*, 2015, **8**, 107101.
40 J.-W. Schüttauf, M. A. Modestino, E. Chinello, D. Lambelet, A. Delfino, D. Dominé, A. Faes, M. Despeisse, J. Bailat, D. Psaltis, C. Moser and C. Ballif, *J. Electrochem. Soc.*, 2016, **163**, F1177.
41 J. Jia, L. C. Seitz, J. D. Benck, Y. Huo, Y. Chen, J. W. D. Ng, T. Bilir, J. S. Harris and T. F. Jaramillo, *Nat. Commun.*, 2016, **7**, 13237.
42 Y. Gao, V. M. L. Corre, A. Gaïtis, M. Neophytou, M. A. Hamid, K. Takanabe and P. M. Beaujuge, *Adv. Mater.*, 2016, **28**, 3366–3373.
43 J. Luo, D. A. Vermaas, D. Bi, A. Hagfeldt, W. A. Smith and M. Grätzel, *Adv. Energy Mater.*, 2016, **6**, 1600100.
44 S. H. Kang, M. J. Jeong, Y. K. Eom, I. T. Choi, S. M. Kwon, Y. Yoo, J. Kim, J. Kwon, J. H. Park and H. K. Kim, *Adv. Energy Mater.*, 2017, **7**, 1602117.
45 B. Weng, F. Xu, C. Wang, W. Meng, C. R. Grice and Y. Yan, *Energy Environ. Sci.*, 2017, **10**, 121–128.
46 W. J. Chang, K.-H. Lee, H. Ha, K. Jin, G. Kim, S.-T. Hwang, H. Lee, S.-W. Ahn, W. Yoon, H. Seo, J. S. Hong, Y. K. Go, J.-I. Ha and K. T. Nam, *ACS Omega*, 2017, **2**, 1009–1018.
47 S.-H. Hsu, J. Miao, L. Zhang, J. Gao, H. Wang, H. Tao, S.-F. Hung, A. Vasileff, S. Z. Qiao and B. Liu, *Adv. Mater.*, 2018, **30**, 1707261.
48 S. Tembhurne, F. Nandjou and S. Haussener, *Nat. Energy*, 2019, **4**, 399–407.
49 S. Muhammad-Bashir, M. Al-Oufi, M. Al-Hakami, M. A. Nadeem, K. Mudiyanselage and H. Idriss, *Sol. Energy*, 2020, **205**, 461–464.
50 J. Liang, X. Han, Y. Qiu, Q. Fang, B. Zhang, W. Wang, J. Zhang, P. M. Ajayan and J. Lou, *ACS Nano*, 2020, **14**, 5426–5434.
51 A. M. Asiri, D. Ren, H. Zhang, S. Bahadar Khan, K. A. Alamry, H. M. Marwani, M. Sherjeel Javed Khan, W. A. Adeosun, S. M. Zakeeruddin and M. Grätzel, *ChemSusChem*, 2022, **15**, e202102471.
52 J. Luo, J.-H. Im, M. T. Mayer, M. Schreier, M. K. Nazeeruddin, N.-G. Park, S. D. Tilley, H. J. Fan and M. Grätzel, *Science*, 2014, **345**, 1593–1596.
53 M. Lee, X. Ding, S. Banerjee, F. Krause, V. Smirnov, O. Astakhov, T. Merdzhanova, B. Klingebiel, T. Kirchartz, F. Finger, U. Rau and S. Haas, *Adv. Mater. Technol.*, 2020, **5**, 2000592.
54 J. W. Ager, M. R. Shaner, K. A. Walczak, I. D. Sharp and S. Ardo, *Energy Environ. Sci.*, 2015, **8**, 2811–2824.
55 J. H. Kim, D. Hansora, P. Sharma, J. W. Jang and J. S. Lee, *Chem. Soc. Rev.*, 2019, **48**, 1908–1971.
56 T. Edvinsson, *Nat. Energy*, 2019, **4**, 354–355.